

# Influence of acidity on liquid–liquid phase transitions of mixed SOA proxy–inorganic aerosol droplets

Yueling Chen<sup>1</sup>& Xiangyu Pei<sup>1</sup>, Huichao Liu<sup>1</sup>, Yikan Meng<sup>1</sup>, Zhengning Xu<sup>1</sup>, Fei Zhang<sup>1</sup>, Chun Xiong<sup>1</sup>, Thomas C. Preston<sup>3</sup>, Zhibin Wang<sup>1,2,4\*</sup>

<sup>1</sup>College of Environmental and Resource Sciences, Zhejiang Provincial Key Laboratory of Organic Pollution Process and Control, Zhejiang University, Hangzhou 310058, China

<sup>2</sup>ZJU-Hangzhou Global Scientific and Technological Innovation Center, Zhejiang University, Hangzhou 311215, China

<sup>3</sup>Department of Atmospheric and Oceanic Sciences and Department of Chemistry, McGill University, 805 Sherbrooke Street West, Montreal, Quebec H3A 0B9, Canada

<sup>4</sup>Key Laboratory of Environment Remediation and Ecological Health, Ministry of Education, Zhejiang University, Hangzhou 310058, China

Correspondence to: Zhibin Wang ([wangzhibin@zju.edu.cn](mailto:wangzhibin@zju.edu.cn))

Yueling Chen and Xiangyu Pei contribute equally to this work.

**Abstract.** Phase state and morphology of aerosol particles play a critical role in determining their effect on climate. While aerosol acidity has been identified as a key factor affecting the multiphase chemistry and phase transitions, the impact of acidity on phase transition of multicomponent aerosol particles has not been extensively studied in situ. In this work, we employ an aerosol optical tweezer (AOT) to probe the impact of acidity on the phase transition behavior of levitated aerosol particles. Our results reveal that higher acidity decreases the separation relative humidity (SRH) of aerosol droplets mixed with ammonium sulfate (AS) and secondary organic aerosol (SOA) proxy, such as 3-methylglutaric acid (3-MGA), 1,2,6-hexanetriol (HEXT) and 2,5-hexanediol (HEXD) across aerosol pH in atmospheric condition. Phase separation of organic acids was more sensitive to acidity compared to organic alcohols. We found the mixing relative humidity (MRH) was consistently higher than the SRH in several systems. Phase-separating systems, including 3-MGA/AS, HEXT/AS, and HEXD/AS, exhibited oxygen-to-carbon ratios (O:C) of 0.67, 0.50, and 0.33, respectively. In contrast, liquid-liquid phase separation (LLPS) did not occur in the high O:C system of glycerol/AS, which had an O:C of 1.00. Additionally, the morphology of 42 out of the 46 aerosol particles that underwent LLPS was observed to be a core-shell. Our findings provide a comprehensive understanding of the pH-dependent LLPS in individual suspended aerosol droplets and pave the way for future research on phase separation of atmospheric aerosol particles.

## 1 Introduction

Atmospheric aerosol particles can directly and indirectly impact climate by absorbing and scattering light and acting as cloud condensation nuclei (Rosenfeld et al., 2014). Particle morphology is a critical factor influencing the physiochemical properties

31 of aerosols such as their optical properties, chemistry, and nucleation processes (Freedman et al., 2009; Corral Arroyo et al.,  
32 2022; Cosman et al., 2008; Lam et al., 2021; Petters and Kreidenweis, 2007; Mikhailov et al., 2021). Morphology can be  
33 broadly categorized into single-phase homogeneous morphology and phase separation morphology (Bertram et al. 2011;  
34 Ciobanu et al. 2009), based on the phase state of the particle. For droplets with a phase separation morphology, the two main  
35 equilibrium morphologies are a fully engulfed (core-shell) structure and a partially engulfed structure (Reid et al. 2011).  
36 Droplets can undergo phase transition processes and thus the morphology would be changed. The composition and mass of  
37 inorganic and organic components impact the phase transition characteristics of a particle. With a decrease of particle water  
38 content, a transition occurs from single homogenous liquid phase to two separated liquid phases, which is known as liquid-  
39 liquid phase separation (LLPS). The relative humidity (RH) when the LLPS occurs is defined as separation relative humidity  
40 (SRH). The reverse process, in which two liquid phases mix into a single homogenous liquid phase, is referred to as liquid-  
41 liquid phase mixing and the corresponding RH is the mixing RH (MRH; You et al., 2014; Gorkowski et al., 2017).

42

43 The phenomenon of LLPS has garnered considerable attention from the atmospheric research community due to its potential  
44 role in affecting the physiochemical properties of atmospheric aerosols (Ott et al., 2020; Freedman, 2020). Song et al. (2012)  
45 using optical microscopy studied the relationship between LLPS and the oxygen-to-carbon ratio (O:C) and discovered that  
46 LLPS was consistently observed when  $O:C < 0.56$ , while it was never observed when  $O:C > 0.80$ . For O:C between 0.56 and  
47 0.80, the occurrence of LLPS was influenced by the types of organic functional groups. Gorkowski et al. (2020) utilized  
48 experimental results of previous studies on LLPS and morphology, observing a general trend in morphology from partially  
49 engulfed to core shell and finally homogeneous as oxidation increased. More recently, it is found that submicrometer-sized  
50 aerosol particles had a lower SRH compared to micrometer-sized droplets (Kucinski et al., 2021; Ohno et al., 2021). Meanwhile,  
51 Stewart et al. (2015) employed aerosol optical tweezer (AOT) to investigate the morphologies of aqueous droplets. They found  
52 in the polyethylene glycol (PEG)/ammonium sulfate (AS) system, droplets formed predominately core-shell particles when  
53 the AS content was high and partially engulfed when the PEG content was high.

54

55 One factor that could influence the phase transitions of aerosol particles is the aerosol pH. The pH values for misty cloud and  
56 fog droplets generally range between 2 and 7, whereas continental and marine aerosol particles exhibit a wider range of pH  
57 values, from -1 to 5 and 0 to 8, respectively (Pye et al., 2020; Angle et al., 2021; Weber et al., 2016; Tilgner et al., 2021; Zheng  
58 et al., 2020). Meanwhile, aerosol pH is size-dependent, with the fine mode showing lower 1–4 pH units than the coarse mode  
59 (Fang et al., 2017; Young et al., 2013; Guo et al., 2017). Losey et al. (2018) studied six organic components and discovered  
60 that phase separation may be hindered by the addition of sulfuric acid, while the SRH of 3-methylglutaric acid/ammonium  
61 sulfate system was found to decrease with the addition of sodium hydroxide (Losey et al. 2016), as the deprotonation of organic  
62 component or difference in salting out ability of inorganic may change the SRH. More recently, Tong et al. (2022) investigated

63 the effect of acidity on phase separation in single suspended microdroplets using AOT. Their results showed that the pH can  
64 affect the miscibility of the mixture and high acidity results in a reduced SRH of 1,2,6-hexanetriol.

65

66 Our aim with this work is to gain a comprehensive understanding of the influence of pH on phase transitions in suspended  
67 droplets. To that end, we investigate pH-dependent SRH and MRH, as well as morphologies of aqueous droplets using AOT,  
68 meanwhile discussed the effect of O:C on phase separation behavior. Compared to substrate-based measurement techniques,  
69 AOT can suspend droplets without any substrate contact, providing a more realistic simulation of the behavior of aerosols in  
70 the atmosphere (Wang et al., 2021; Cui et al., 2021; Redding et al., 2015; Gong et al., 2018; Rafferty et al., 2023). We measured  
71 droplets containing AS and a range of organic compounds with varying O:C. We discuss how our findings provide insight into  
72 the mechanisms behind pH-dependent phase transitions in levitated droplets, along with the implications for fields such as  
73 climate science. Overall, our study highlights the importance of considering pH as a key factor in the phase transition behavior  
74 of micron-sized droplets and underscores the need for further research to fully understand the complex interactions between  
75 pH and phase transitions in these atmospherically relevant systems.

## 76 **2 Methods**

### 77 **2.1 Aerosol generation**

78 Four organics components: glycerol (GL), 3-methylglutaric acid (3-MGA), 1,2,6-hexanetriol (HEXT), and 2,5-hexanediol  
79 (HEXD), were chosen because they are commonly-used secondary organic aerosol (SOA) proxies (Lam et al., 2021;  
80 Gorkowski et al., 2020). O:C of the selected chemicals varied from 1 to 0.33 (**Table 1**), which is similar to the real  
81 atmospheric SOA (Canagaratna et al., 2015; Mahrt et al., 2021). AS was chosen as the inorganic salt component due to its  
82 widespread occurrence in the atmospheric environment. All concentrations of organics and AS in the mother solutions were  
83 50 g/L. The pure organic and inorganic components were dissolved in ultrapure water (Millipore, resistivity of 18.2 M $\Omega$ ) to  
84 create solutions with organic-to-inorganic mass ratio (OIR) of 1:1. The pH of studied system were adjusted within the range  
85 of 0.48 to 6.53 by using either concentrated sulfuric acid (SA) or sodium hydroxide (NaOH) solution (5.29 mol/L). Sodium  
86 hydroxide, a strong base, allowed for pH adjustment with minimal usage (Losey et al., 2016). However, it is necessary to  
87 acknowledge that the addition of NaOH changes the composition of the inorganic part of the solution, potentially affecting the  
88 SRH values measured. For the 3-MGA/AS system, either SA or NaOH was utilized, while for the HEXT/AS and HEXD/AS  
89 systems, only SA was used. The pH of each solution was measured using a pH meter (Mettler Toledo Instruments Co., Ltd.,  
90 Shanghai, China). The purity and supplier of the compounds used in this study were summarized in **Table S1**.

91

**Table 1.** Information of the solutions used to generate aerosol droplets.

| Solution ID | Organic component     | O:C ratio | pH        |
|-------------|-----------------------|-----------|-----------|
| GL          | glycerol              | 1.00      | 5.24±0.01 |
| 3-MGA-I     | 3-methylglutaric acid | 0.67      | 0.48±0.01 |
| 3-MGA-II    |                       |           | 1.19±0.01 |
| 3-MGA-III   |                       |           | 2.70±0.01 |
| 3-MGA-IV    |                       |           | 3.70±0.01 |
| 3-MGA-V     |                       |           | 5.21±0.02 |
| 3-MGA-VI    |                       |           | 6.53±0.02 |
| HEXT-I      | 1,2,6-hexanetriol     | 0.50      | 0.92±0.01 |
| HEXT-II     |                       |           | 2.02±0.01 |
| HEXT-III    |                       |           | 3.14±0.01 |
| HEXT-IV     |                       |           | 5.11±0.02 |
| HEXD-I      | 2,5-hexanediol        | 0.33      | 1.39±0.01 |
| HEXD-II     |                       |           | 2.03±0.01 |
| HEXD-III    |                       |           | 2.71±0.01 |
| HEXD-IV     |                       |           | 3.13±0.01 |
| HEXD-V      |                       |           | 5.01±0.01 |

92

## 93 2.2 Experimental setup

94 A schematic illustration of the experimental setup is presented in **Fig. S1**. The aerosol optical tweezer system consists of a  
95 custom-made levitation chamber that integrates the optical trapping system, the illumination and imaging system, and the  
96 aerosol generation system. A 532 nm (Opus 532-2W) laser was used to create an optical trap with a 100x oil immersion  
97 objective (Olympus, UPLFLN100XO, NA 1.30) pressed against a glass coverslip (Nest, thickness 160-190  $\mu\text{m}$ ). The  
98 illumination and imaging system includes a 450 nm LED (Daheng Optics, GCI060404) and a camera (Thorlabs, CS165CU/M)  
99 to illuminate and image the particle. Two low pass filters (Andover, 500FL07-25) were used in front of the camera lens to  
100 remove the influence of back scattered light of the 532 nm laser to photograph clear image of the particle. The Raman scattered  
101 light passed through two 50:50 beam splitters (CVI Laser Optics, BTF-VIS-50-2501M-C) and a notch filter (Semrock, NFD01-  
102 532-25x36) and was focused into the Raman spectrograph. A spectrograph (ZOLIX, Omni- $\lambda$ 5004i) is used to measure the  
103 Stokes shifted Raman spectrum. A 20  $\mu\text{m}$  entrance slit width and 1200 groove/mm diffraction grating with blaze wavelength  
104 of 500 nm were used to achieve a spectral resolution of 0.021 nm. The wavelength position of spectrograph was calibrated  
105 with Hg-laser. The Raman scattered light was recorded every 4 second with range of 624.24-665.40 nm.

106

107 As droplets are introduced continuously into the chamber from a medical nebulizer (LANDWIND, PN100), smaller droplets  
108 undergo a process of collision and coalescence, leading to the formation of larger droplets that can be readily trapped near the  
109 focal point of the laser. In most cases, droplets can be successfully captured within 30 s after the introduction of an aerosol  
110 plume into the cell. Air with relative humidity (RH) of 100% and 0% were mixed to produce wet air with a desired RH. The  
111 flow rates of the humidified and dry air streams were regulated by mass flow controllers (MFCs, Tianjin Gastool Instruments  
112 Co., Ltd., Tianjin, China, GT130D), with a combined flow rate of 0.3 L/min in total. Two humidity sensors (Sensirion, SHT85)  
113 were utilized, with a precision of  $\pm 1.5\%$ . Since the sensor located behind the chamber was positioned in close proximity ( $\sim 80$   
114 mm) to the droplet, its observed values were used as a surrogate for measuring the RH inside the chamber. The RH values  
115 were reduced in increments of 5% every 30 minutes (Tong et al., 2022; Stewart et al., 2015) until droplet phase separation  
116 occurred. The measured values of RH given by the sensors were used as the phase separation RH. Subsequently, the RH level  
117 was set to 100%, to investigate the phase mixing of the droplets. The entire experiment was repeated 2~4 times for each system.

### 118 **2.3 Determination of phase transitions**

119 When a transparent or weakly absorbing spherical particle is trapped, it can behave as a high-quality factor optical cavity that  
120 supports sharp optical resonances, resulting in cavity-enhanced Raman scattering. These resonances can be observed as peaks  
121 in the Raman spectrum of a particle and are often referred to as whispering gallery modes (WGMs). In principle, particle  
122 morphology can be deduced from the WGMs, as inhomogeneities in the refractive index can disrupt the circulation of the  
123 WGMs (Lin et al., 1992; Mitchem et al., 2006). Raman spectra measurements of single droplets in various morphological  
124 states are presented in **Figure 1**. When the droplet was in a homogeneous phase morphology, the droplet acted as a high-  
125 quality microcavity and sharp WGM peaks overlapped with the spontaneous Raman spectrum (**Fig. 1a**). When the droplet was  
126 in a state of a core-shell structure, observed WGMs were clearly diminished in measured spectra (**Fig. 1b**). The origin of the  
127 damping of the WGMs is the radial homogeneity that is present when the particle is separated into a hydrophilic core and a  
128 hydrophobic shell. As a result, when fitting the Raman spectra with the Mie scattering model for homogeneous droplets, the  
129 error in the best-fits greatly increase. Examination of the retrieved radius and refractive index reveals a clear break with fits  
130 for that of a homogeneous sphere. Therefore, the point at which a significant break in particle size and refractive index occurred  
131 can be used as the point at which core-shell phase separation occurs. As illustrated in **Fig. 1c**, when the droplet was partially-  
132 engulfed and non-spherical, WGM peaks in the spectrum are absent (Reid et al., 2011). The origin of the spontaneous Raman  
133 peaks at  $3300\text{ cm}^{-1}$  and  $\sim 3050\text{ cm}^{-1}$  are identified as the spurious or weakened WGM peaks and the vibration of N-H bond,  
134 respectively. Overall, the results of this analysis demonstrate the dynamic changes in the Raman spectra of single droplets as  
135 they undergo morphological transitions (Sullivan et al., 2020; Stewart et al., 2015; Tong et al., 2022).

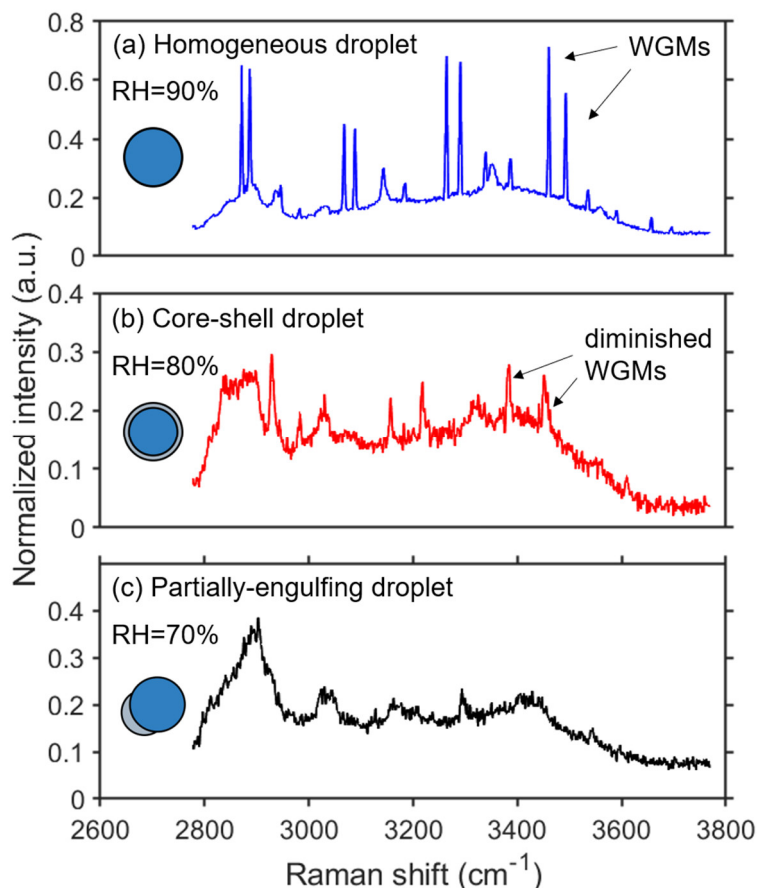


**Figure 1.** Raman spectra of 3-MGA-II microdroplets: (a) a homogenous droplet (RH = 90%); (b) a core-shell droplet (RH = 80%); (c) a partially-engulfed droplet (RH=70%). The WGMs are marked by black arrows. The normalization of the peak is achieved by dividing it by the maximum value of the spectrum's intensity, respectively.

The peak finding method used in this study is based on the `ipeak` code developed by O'Haver (2022). In short, the code first smooths the first derivative of the signal and identified downward-going zero-crossings that met a certain predetermined minimum slope and amplitude threshold. By adjusting the corresponding parameters, it is possible to accurately detect the desired peaks. The algorithm used to fit WGM peaks in spectra from homogenous spheres in this study was proposed by Preston and Reid (2013) and Preston and Reid (2015). The algorithm compares observed peak positions to expected positions calculated using a resonance condition from Mie theory. Error is minimized by varying particle size and refractive index (i.e. the parameters of best-fit). The method has been demonstrated to provide a rapid determination of the fitted radius and refractive index with an accuracy of  $\pm 2$  nm and  $\pm 0.0005$ , respectively. During the experiment with reduced RH, we had to adjust the laser power to ensure the stable capture of droplets, which will affect the peak intensity. To eliminate this effect, as

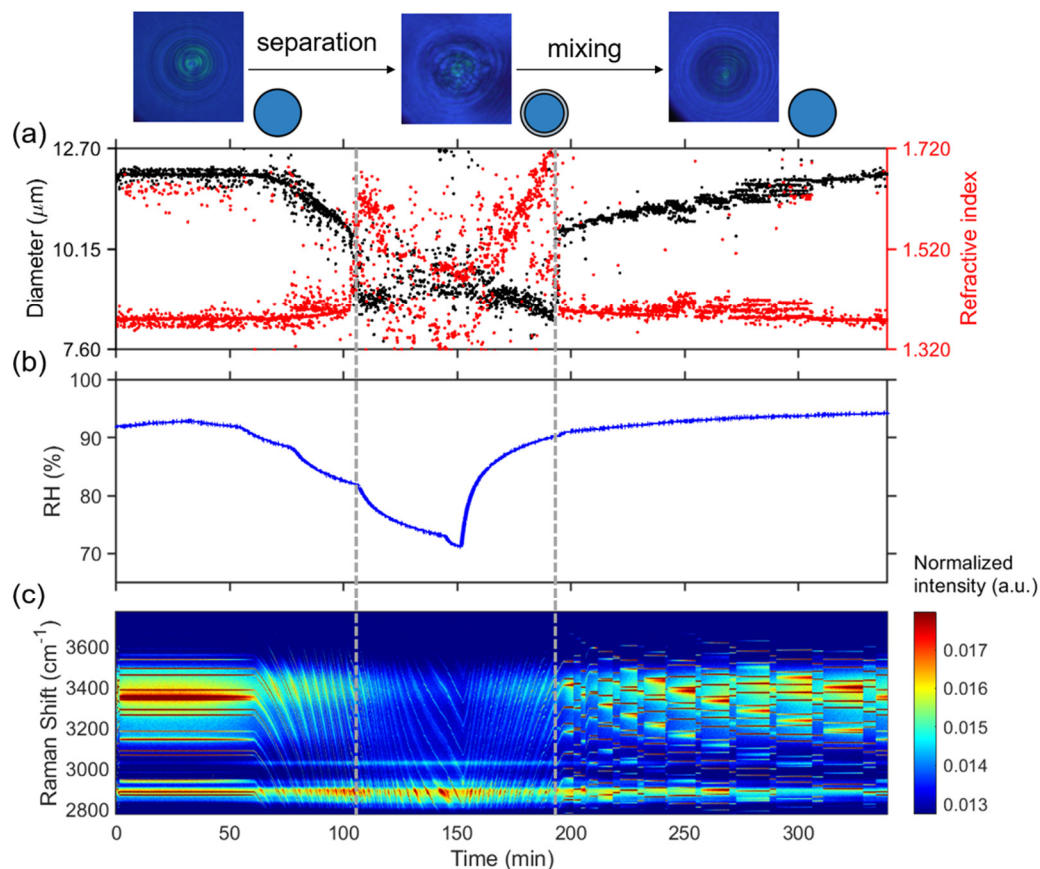
150 demonstrated by Tong et al. (2022), we normalized all Raman spectra used in this study by the area below the spontaneous  
151 Raman signals.

## 152 **3 Results and discussion**

### 153 **3.1 Phase behaviors of droplets mixed SOA proxy with AS**

154 **Fig. 2** presents the results of time-resolved Raman spectra of aerosol droplets produced from a 3-MGA-II solution under  
155 continuously varying RH, as well as the corresponding particle size and refractive index values. To enable temperature and  
156 RH to stabilize, the chamber was conditioned with airflow for 50 minutes after trapping a particle. During the dehumidification  
157 process, the particle diameter decreased from 11.85  $\mu\text{m}$  to 9.03  $\mu\text{m}$  and the refractive index increased from 1.379 to 1.475  
158 when RH decreased from 93.0% to 70.0%. The particle size and water content decreased with RH due to the equilibrium  
159 partitioning of water molecules between vapor and droplets. Meanwhile, the refractive index of the droplets gradually increased  
160 as the water content decreases. When LLPS occurred, the droplets changed from a symmetrical homogeneous phase to either  
161 an asymmetrical partially engulfed structure which led to the disappearance of the WGMs, or the formation of a core-shell  
162 structure. As RH in the reaction chamber was reduced, the LLPS was initiated, marked by the variations of the WGM signal  
163 (See **Fig. 1b**). This was achieved by reducing setting RH (setting values) by 5% at 30-minute intervals until the organic phase  
164 separated from the water-rich phase and then continuing decreasing RH by 10%-15%. **Fig. 2a** illustrates how the fitting of the  
165 droplet diameter and the refractive index deteriorated as the shell develops, indicating phase separation. The refractive index's  
166 shift results from a significant change in the radial profile due to the formation of a core-shell structure. Additionally, the  
167 persistence of strong WGMs indicates that the morphology of the droplet remains spherical following LLPS and is core-shell.  
168 During the RH increased from 70% to 95%, the reappearance of the continuously shifting WGM signal is observed, suggesting  
169 that the inorganic phase has mixed with the organic phase, and droplet returned to a homogeneous phase. During the  
170 humidification process, there is an opposite trend observed in the particle size and refractive index of the droplet compared to  
171 the dehumidification process. In conclusion, the variations of the WGM signal can serve as a reliable indicator of the  
172 occurrence of liquid-liquid phase separation or mixing, and the RH at these points can be considered as the SRH or MRH,  
173 respectively. The observed phase transitions of droplets produced from HEXT-IV and HEXD-V solutions were shown in **Fig.**  
174 **3** and **Fig. 4** respectively.

175

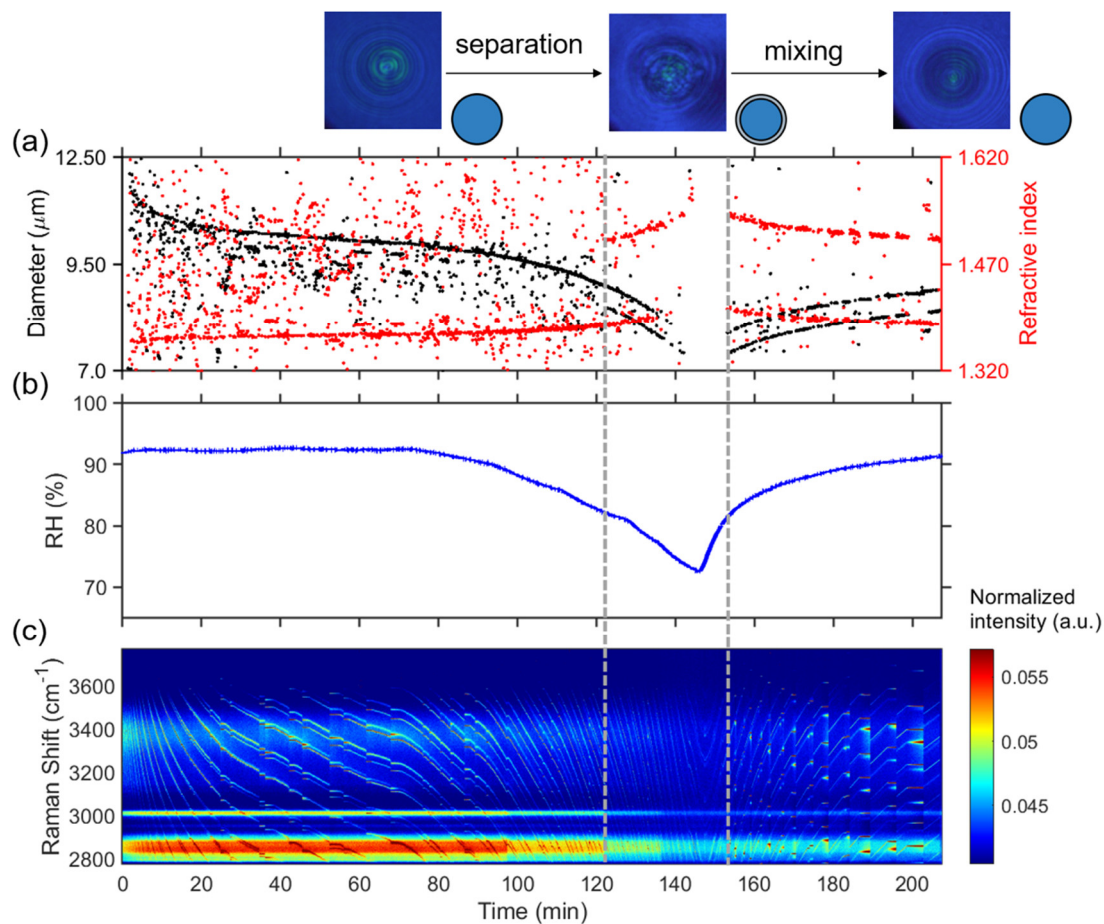


176

177 **Figure 2.** Liquid-liquid phase separation and mixing of aqueous 3-MGA-II. Schematic diagram of phase states is on the top  
 178 of the figure. (a) Timescale of changes in droplet size and refractive index, determined from fitting the Raman shift positions  
 179 of the WGMs. (b) RH variation after the trapping chamber during the humidity changing process. (c) Time-resolved Raman  
 180 spectra. The cessation of the random motion of inclusions within the droplet and the resultant formation of a core-shell  
 181 structure are indicated by the grey dashed line on the left. The grey dashed line on the right serves as an indication of the point at which  
 182 the droplet morphology transitioned from a state of separated phases to a homogeneous phase. The Raman spectra at 53 min, 113  
 183 min, 130 min are shown in **Fig. 1(a), (b), (c)**, respectively. Fitting errors of the WGMs were presented in **Fig. S3**.

184

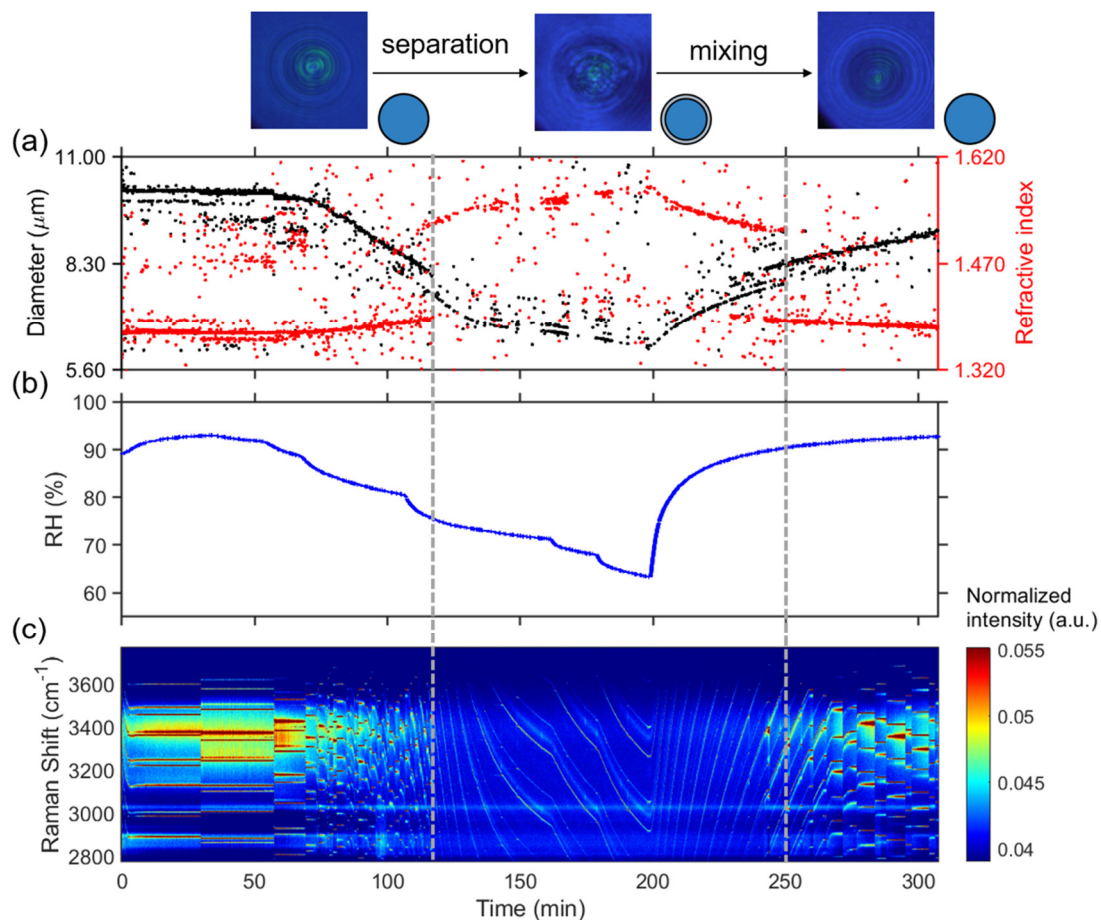




185

186 **Figure 3.** Liquid-liquid phase separation of aqueous of HEXT-IV. (a) Timescale of changes in droplet size and refractive index,  
 187 determined from fitting the Raman shift positions of the WGMs. (b) RH variation after the trapping chamber during the  
 188 humidity changing process with time. (c) Time-resolved Raman spectra. The cessation of the random motion of inclusions  
 189 within the droplet and the resultant formation of a core-shell structure are indicated by the grey dashed line on the left. The  
 190 grey dashed line on the right serves as an indication of the point at which the droplet morphology transitions from a state of  
 191 phase separation to a homogeneous phase morphology. This transformation is characterized by the occurrence of phase mixing.

192



193

194 **Figure 4.** Liquid-liquid phase separation of aqueous of HEXD-V. (a) Timescale of changes in droplet size and refractive index,  
 195 determined from fitting the Raman shift positions of the WGMs. (b) RH variation after the trapping chamber during the  
 196 humidity changing process. (c) Time-resolved Raman spectra. The cessation of the random motion of inclusions within the  
 197 droplet and the resultant formation of a core-shell structure are indicated by the grey dashed line on the left. The grey dashed  
 198 line on the right serves as an indication of the point at which the droplet morphology transitions from a state of phase separation  
 199 to a homogeneous phase morphology. This transformation is characterized by the occurrence of phase mixing.

200

201 **Fig. S2** presents the results of time-resolved Raman spectra of aerosol droplets produced from GL/AS solution under  
 202 continuously varying RH, as well as the corresponding particle diameter and refractive index values. At the start of the  
 203 experiment, the chamber RH was held at 93% for approximately 75 minutes. The spectrum during this period reveals a clear  
 204 bright trend, indicative of the presence of many WGMs in the newly captured droplets. As the chamber RH dropped to a  
 205 minimum value of 71.5% at around 200 minutes, the position of the WGMs in each spectral snapshot shifted continuously,  
 206 following the same trend as the chamber RH. This observation suggests that the droplet was homogeneous and that no phase

207 separation occurred in the experimental RH range. The phenomenon regarding the GL/AS system is consistent with the  
208 conclusion by Song et al. (2013) and Gorkowski et al. (2020).

### 209 **3.2 Effect of pH on SRH and MRH of different systems**

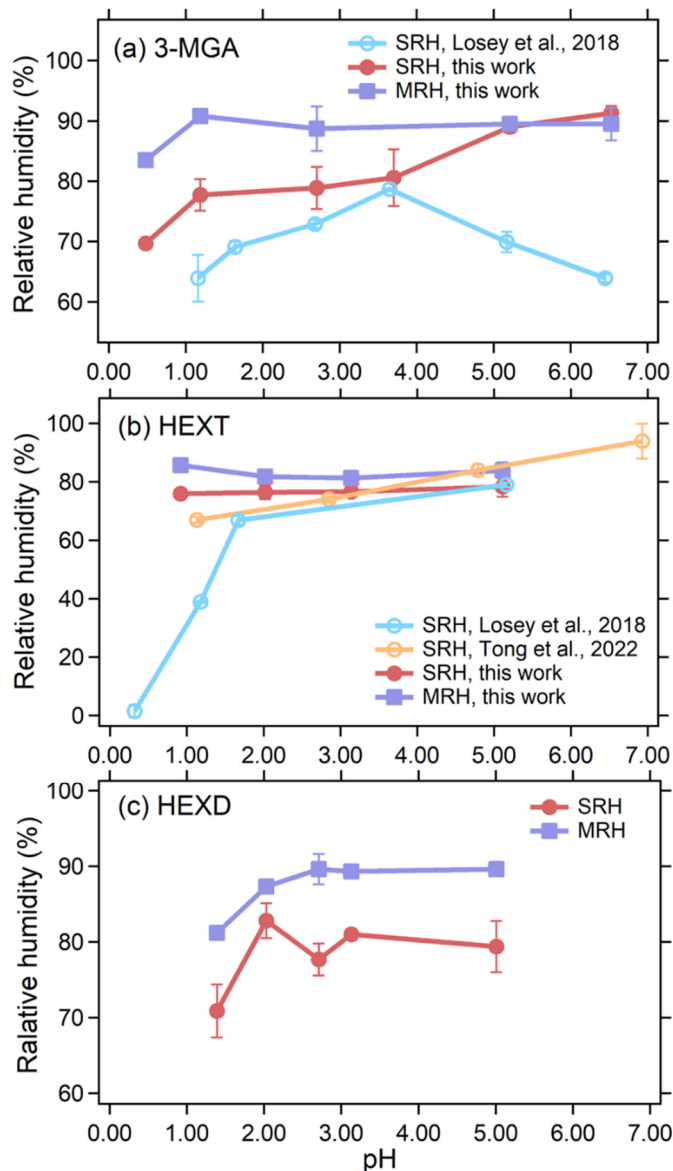
210 The SRH and MRH of aerosol droplets produced from 3-MGA-I~VI solution are shown in **Fig. 5a** and **Table S2**. The SRH  
211 values were 92.7%, 89.5%, 80.6%, 79.7%, 76.2% and 69.7% at pH of 6.53, 5.21, 3.70, 2.70, 1.19 and 0.48, respectively. It is  
212 worth mentioning that when the pH of the 3-MGA system is 0.48, only two sets of valid parallel experimental data are available,  
213 even though we had repeated the experiment several times. Because in other parallel experiments, the SRH of the droplet is  
214 lower than the capture range of AOT, the AOT would not be able to continue the capture when the particle size decreases to  
215  $\sim 6 \mu\text{m}$ . Therefore, the actual SRH may be a bit lower at this pH, but this does not affect the results we discuss later. With a  
216 decrease in pH, ammonium sulfate transforms into ammonium bisulfate. Predicted by the Hofmeister series, ammonium  
217 bisulfate exhibits a weaker salting out effect compared to ammonium sulfate and thus hinders the ability of organic matter to  
218 precipitate out of the solution (Losey et al., 2018). The MRH values at pH 6.53, 5.21, 2.70, 1.19 and 0.48 were 87.6%, 89.5%,  
219 87.3%, 83.9% and 83.5%, respectively, and are generally higher than corresponding SRH, especially in the low pH range  
220 ( $< 5.00$ ). The hysteresis between SRH and MRH existed because the SRH process has an activation barrier while the MRH  
221 process does not, and lower RH is needed for the aerosol droplet to overcome the activation barrier to form two phases  
222 (Freedman, 2020). Similar results were also observed in HEXT/AS and HEXD/AS systems. Additionally, the pH-dependent  
223 SRHs obtained in this study were compared to those reported by Losey et al. (2018), as depicted in **Fig. 5a**. It is worth  
224 mentioned that the solute concentration used in our study (50g/L) is comparable to Losey et al. (2018) (5.0 wt%), allowing for  
225 meaningful comparison of results. Overall, the SRHs of 3-MGA obtained in this study was higher than the results of Losey et  
226 al. (2018). When the pH was lower than 3.70, in 3-MGA system, the present study followed a similar trend as the results of  
227 Losey et al. (2018), with the SRH decreasing as the pH decreased. However, when the pH was greater than 3.70, our study  
228 showed an opposite trend compared to the results of Losey et al. (2018). The observed discrepancy may be attributed to the  
229 distinct ambient conditions of the droplets. The laser levitation, resulting in a spherical morphology, while the optical  
230 microscopy involves substrate deposition, leading to a morphology resembling a spherical crown (Tong et al., 2022; Zhou et  
231 al., 2014). The underlying reasons for these differences are currently unclear, and further investigations are needed.

232  
233 In addition to 3-MGA, we also studied two organic/AS systems to investigate how acidity affects SRH and MRH of aerosols  
234 of differing composition. These results are shown in **Fig. 5** and tabulated in **Table 2**. The separation diameter (SD) of 3-  
235 MGA/AS ranges from  $7.23 \mu\text{m}$  to  $9.74 \mu\text{m}$ , with a corresponding separation refractive index (SRI) ranging from 1.362 to 1.515.  
236 For HEXT/AS, the SD ranges from  $9.01 \mu\text{m}$  to  $9.90 \mu\text{m}$ , while the SRI ranges from 1.396 to 1.421. Lastly, the SD of HEXD/AS  
237 ranges from  $7.45 \mu\text{m}$  to  $8.97 \mu\text{m}$ , with the SRI ranging from 1.382 to 1.406. The data suggests that acidity did not have a  
238 noticeable effect on the MRH of the various systems. The pH of the HEXT/AS solution without the addition of any acid was

239 5.11, and sulfuric acid was utilized to adjust the pH to lower levels (3.14, 2.02 and 0.92). The SRH values of HEXT/AS system  
240 (O:C=0.50) decreased as the pH decreased, with values of 78.3%, 76.6%, 76.4% and 75.7% at pH values of 5.11, 3.14, 2.02  
241 and 0.92, respectively. The trend is similar to the 3-MGA (O:C=0.67) system, and the reason why SRH decreased may be due  
242 to the acid enhancing the miscibility of organic alcohols and inorganic substances, resulting in a greater difficulty in separating  
243 the hydrophobic phase from the water-rich phase (Tong et al., 2022). Still, we observed SRH was not strongly dependent on  
244 pH for HEXT/AS, compared to 3-MGA/AS system. This is likely due to the fact that organic alcohols have a large  $pK_a$  (e.g.  
245 the  $pK_a$  of HEXT is 14.3) and therefore exhibit minimal ionization in the pH range studied here (Wade and Simek, 2020).  
246 Additionally, the relative molecular interactions between alcohols and water are weaker than those of acids, leading to a weaker  
247 dependence of salting out ability of AS in the HEXT/AS system. The results of Losey et al. (2018) and Tong et al. (2022) were  
248 also depicted in **Fig. 5b**. Our results differ from those of Losey et al. (2018), who observed a significant decline in SRH as the  
249 pH decreased. The specific reason for the discrepancy remains unclear, but we speculate it may due to different condition of  
250 droplet. Moreover, the concentration of HEXT in this work (50g/L) is higher than concentration (2.5 wt%, about 26 g/L) of  
251 Losey et al. (2018). The higher concentration may enhance the precipitation of organic matter from the inorganic salts in our  
252 work. In contrast to the findings of Tong et al. (2022), our study observed a less pronounced trend in the values of SRH, and  
253 a narrower range in the distribution of SRH compared to literature values. The difference in OIR between this study (1:1) and  
254 Tong et al. (2022) (2:1) may account for the discrepancy in SRH. Previous studies (Ma et al., 2021; Stewart et al., 2015; Song  
255 et al., 2012) indicated that OIR differences could affect SRH, but SRH was not significantly dependent on OIR. The  
256 discrepancy in SRH may also be due to the variations in experimental conditions, such as laser power, experimental duration,  
257 etc. For HEXD/AS (O:C=0.33) system, SRH decreases significantly when the pH is less than 2.00, while acidity had no  
258 significant effect on SRH when pH is greater than 2.00, with values of 79.4%, 81.0%, 77.7%, 82.8% and 70.9% at pH values  
259 of 5.01, 3.13, 2.71, 2.03 and 1.39, respectively. This phenomenon was attributed to a mechanism similar to that observed in  
260 HEXT/AS. To our knowledge, this is the first investigation on the pH-dependent phase transition of HEXD/AS at the single  
261 particle level in a contact-free environment.

262  
263 The pH values of misty cloud and fog droplets typically fall within the range of 2 to 7, whereas continental and marine aerosol  
264 particles display a broader spectrum of pH values (Pye et al., 2020; Tilgner et al., 2021). Our research suggests that in real  
265 atmospheric conditions, phase separation behavior of droplets may be influenced significantly by their acidity. It is challenging  
266 to measure the droplet pH of the investigated system using AOT. However, previous studies (Coddens et al., 2019; Li et al.,  
267 2023) have shown that at high RH (90%~100%), the difference in the pH values between droplets and bulk solution is relatively  
268 small. Therefore, we used bulk solution pH as an indicator of pH at droplet phase transition. This study focused on volatile  
269 organics and was conducted over a relatively long period, which may have affected our results. Nevertheless, the organic  
270 compounds used in this study have low volatility. For instance, the vapor pressure of 3-MGA is  $7.41 \times 10^{-7}$  to  $2.92 \times 10^{-4}$  mmHg  
271 (DTXSID50871000, United States Environmental Protection Agency), compare to normal volatile organic components of

272 atmospheric aerosol, such as 2-Methyl-1-propanol with vapor pressure of 10.5 to 16.4 mmHg (DTXSID0021759, United States  
 273 Environmental Protection Agency). Volatility information of other organics are provided in the Table S5. Also, the influence  
 274 of droplet size change in our system can be neglected. For example, as shown in **Fig. 2**, the droplet size is basically same at  
 275 the beginning and the end of the experiment at the same RH 93.0% (11.85  $\mu\text{m}$  at the beginning and 11.79  $\mu\text{m}$  at the end).  
 276



277  
 278 **Figure 5.** SRHs and MRHs as a function of pH for (a) 3-MGA/AS system, (b) HEXT/AS system, (c) HEXD/AS system.  
 279 Hollow circles represent data from Losey et al. (2018) and Tong et al. (2022). The error bars of SRHs and MRHs are derived  
 280 from multiple measurements.

281 **Table 2.** SRH information for each pH studied as well as initial diameter, separation diameter (SD), separation refractive index  
 282 (SRI), MRH, mixing diameter (MD), and mixing refractive index (MRI) data.

| 3-MGA/AS system (O:C=0.67) |                                   |                |                      |                                 |                |                      |                                 |
|----------------------------|-----------------------------------|----------------|----------------------|---------------------------------|----------------|----------------------|---------------------------------|
| Initial pH                 | Initial Diameter( $\mu\text{m}$ ) | SRH (%)        | SD ( $\mu\text{m}$ ) | SRI ( $\lambda=650\text{ nm}$ ) | MRH (%)        | MD ( $\mu\text{m}$ ) | MRI ( $\lambda=650\text{ nm}$ ) |
| 0.48                       | 10.97 $\pm$ 1.57                  | 69.7 $\pm$ 0.2 | 7.23 $\pm$ 1.72      | 1.515 $\pm$ 0.086               | 83.5           | 6.82                 | 1.540                           |
| 1.19                       | 11.23 $\pm$ 1.20                  | 77.7 $\pm$ 2.6 | 8.68 $\pm$ 2.38      | 1.454 $\pm$ 0.100               | 90.8 $\pm$ 0.2 | 9.08 $\pm$ 1.64      | 1.394 $\pm$ 0.009               |
| 2.70                       | 12.02 $\pm$ 2.94                  | 78.9 $\pm$ 3.5 | 7.88 $\pm$ 1.21      | 1.493 $\pm$ 0.082               | 88.7 $\pm$ 3.7 | 6.81 $\pm$ 2.76      | 1.506 $\pm$ 0.094               |
| 3.70                       | 10.87 $\pm$ 1.87                  | 80.6 $\pm$ 4.7 | 7.24 $\pm$ 1.00      | 1.491 $\pm$ 0.088               |                |                      |                                 |
| 5.21                       | 11.06 $\pm$ 1.63                  | 89.0 $\pm$ 0.9 | 8.93 $\pm$ 0.16      | 1.362 $\pm$ 0.014               | 89.5           | 7.89                 | 1.381                           |
| 6.53                       | 13.73 $\pm$ 0.41                  | 91.3 $\pm$ 1.2 | 9.74 $\pm$ 0.36      | 1.444 $\pm$ 0.187               | 89.5 $\pm$ 2.7 | 7.89 $\pm$ 0.06      | 1.383 $\pm$ 0.01                |
| HEXT/AS system (O:C=0.50)  |                                   |                |                      |                                 |                |                      |                                 |
| 0.92                       | 13.52 $\pm$ 1.6                   | 75.9 $\pm$ 0.2 | 9.90 $\pm$ 0.76      | 1.421 $\pm$ 0.017               | 85.7           | 10.83                | 1.420                           |
| 2.02                       | 12.88 $\pm$ 1.0                   | 76.4 $\pm$ 2.3 | 9.09 $\pm$ 0.46      | 1.409 $\pm$ 0.007               | 81.8           | 9.34                 | 1.410                           |
| 3.14                       | 12.31 $\pm$ 0.8                   | 76.6 $\pm$ 1.5 | 9.01 $\pm$ 0.47      | 1.408 $\pm$ 0.002               | 81.3           | 9.04                 | 1.409                           |
| 5.11                       | 13.53 $\pm$ 0.4                   | 78.3 $\pm$ 3.4 | 9.15 $\pm$ 0.35      | 1.396 $\pm$ 0.014               | 83.9 $\pm$ 2.8 | 9.04 $\pm$ 0.73      | 1.412                           |
| HEXD/AS system (O:C=0.33)  |                                   |                |                      |                                 |                |                      |                                 |
| 1.39                       | 11.48 $\pm$ 0.78                  | 70.9 $\pm$ 3.5 | 7.45 $\pm$ 0.77      | 1.406 $\pm$ 0.008               | 81.2           | 7.93                 | 1.406                           |
| 2.03                       | 10.54 $\pm$ 0.57                  | 82.8 $\pm$ 2.3 | 7.90 $\pm$ 0.99      | 1.382 $\pm$ 0.007               | 87.3           | 8.83                 | 1.392                           |
| 2.71                       | 14.55 $\pm$ 1.36                  | 77.7 $\pm$ 2.1 | 8.30 $\pm$ 0.28      | 1.391 $\pm$ 0.009               | 89.6 $\pm$ 2.0 | 8.53 $\pm$ 0.32      | 1.388 $\pm$ 0.010               |
| 3.13                       | 11.02 $\pm$ 0.62                  | 81.0 $\pm$ 0.7 | 8.97 $\pm$ 0.22      | 1.384 $\pm$ 0.016               | 89.3           | 9.14                 | 1.384                           |
| 5.01                       | 12.22 $\pm$ 2.73                  | 79.4 $\pm$ 3.4 | 8.33 $\pm$ 0.40      | 1.384 $\pm$ 0.019               | 89.6 $\pm$ 0.1 | 8.38 $\pm$ 0.54      | 1.390 $\pm$ 0.004               |

283

### 284 3.3 Effect of O:C on phase separation behavior in different systems

285 Our findings provide evidence that phase separation of droplets persists even when the organic-inorganic system is adjusted  
 286 to a specific level of acidity. An important determinant of whether droplets undergo phase separation is the O:C. To illustrate  
 287 this, we have included a plot in **Fig. S4**, which show cases the experimental system used in our study alongside relevant  
 288 literature values. One point that needs to be declared is **Fig. S4** only plotted for systems with no additional H<sub>2</sub>SO<sub>4</sub> or NaOH.  
 289 As shown in **Fig. S4**, our findings, as well as those from previous studies (You et al., 2013; O'Brien et al., 2015), indicated  
 290 that there is no correlation between the occurrence of LLPS and the hydrogen-to-carbon (H:C) ratios of the organics, which is  
 291 consistent with results in previous findings (Bertram et al., 2011; Song et al., 2012). However, a clear trend was observed  
 292 between LLPS occurrence and the O:C of the organic components. We observed that droplets of 3-MGA/AS, HEXT/AS and  
 293 HEXD/AS systems with O:C between 0.33 and 0.67 undergo LLPS. With the decrease of water content in the droplets, two  
 294 distinct phases were formed: an organic-rich phase and a salt-rich aqueous phase, under both acidic and neutral conditions. By  
 295 contrast, no LLPS occurred in the GL/AS system, as shown in **Fig. S2**. In general, particles with low O:C are more prone to

296 undergo LLPS. This observation is consistent with the findings of Song et al. (2012) who reported that LLPS was never  
297 observed when O:C > 0.80 and always observed when O:C < 0.56.

298

299 As shown in **Fig. 2** and **Table S2**, for most spectra, WGMs remained after LLPS occurred for droplets of 3-MGA/AS. This  
300 phenomenon indicated that the droplets undergo LLPS with a core-shell morphology in most conditions, which is consistent  
301 with the prediction of Gorkowski et al. (2020). Meanwhile, morphology of phase-separated droplets containing either HEXT  
302 or HEXD were also core-shell shape mostly, as depicted in **Fig. 3/4** and **Table S3/S4**. It is attributed to the lower interfacial  
303 tension observed at higher O:C, leading to higher possibility condition for forming core-shell shaped droplets (Gorkowski et  
304 al., 2020). These findings support the idea that the O:C plays a crucial role in determining the morphology of phase-separated  
305 particles in organic/inorganic mixed aerosols.

#### 306 **4 Conclusion**

307 The aim of this study was to investigate the effect of pH and O:C on phase transition behavior of levitated particles using the  
308 AOT. Our results show that across aerosol pH in atmospheric condition, the presence of sulfuric acid inhibited the LLPS of  
309 aerosol droplets that contained organics (3-MGA, HEXT, HEXD) and AS. Additionally, the MRHs were found to be higher  
310 than the SRHs. The O:C of phase-separating systems is 0.67, 0.50, 0.33, and by contrast, LLPS of the high O:C system (GL,  
311 O:C=1.00) did not occur. Meanwhile, the morphology of levitated aerosol particles was studied and we found that 42 out of  
312 46 droplets that underwent LLPS for a core-shell structure. The SRH of all experimental systems ranged from ~70% to 90%.  
313 In certain cases, as the RH decreased, the droplet morphology changed from core-shell to partially engulfed, similar to the  
314 findings reported by Kucinski et al. (2020). However, as the RH further decreased, the droplet particle size became smaller  
315 than 6  $\mu\text{m}$ , making it impossible to capture them using AOT. Consequently, in most instances, we were unable to observe the  
316 droplet morphology at RH levels below 70%. The results presented here provide new insights into the behavior of different  
317 types of aerosol droplets, and the findings have important implications for our understanding of physical and chemical  
318 processes that occur in the atmosphere. It is anticipated that future studies will be carried out to examine the OIR-dependent  
319 phase separation in real acidified ambient aerosols. Such research will provide insights into the morphological characteristics  
320 of real aerosols and the ways in which these characteristics influence important properties such as hygroscopicity and  
321 homogenous chemistry. Such information will be helpful in furthering our understanding of the impacts of ambient aerosols  
322 on the environment and human health.

323

324 Additionally, in-situ measurement or pH estimation methods, such as the real-time AOT analysis in microdroplets reported  
325 by Boyer et al. (2020) could be combined with SRH measurements for a more accurate and comprehensive analysis.

326 Furthermore, our study used a surrogate for SOA instead of in situ measurements of real SOA, which can be addressed in  
327 future work using SOA generated from a smog chamber or real SOA precursors and oxidized species.

328

329 **Data availability.** The data used in this paper can be obtained from the corresponding author upon request.

330 **Author contributions.** YC built the instrument, performed the experiments, analyzed the data, plotted the figures, and wrote  
331 the original draft. XP conceptualized the study, contributed to instrumentation, data analysis, discussion, and reviewed the  
332 manuscript. HL and CX contributed to the instrumentation and discussion. YM contributed to the experiments and discussion.  
333 ZX, FZ contributed to the discussion and manuscript review. TCP contributed to data analysis and manuscript review. ZW  
334 administrated the project, conceptualized the study, reviewed the manuscript, and contributed to funding acquisition.

335 **Competing interests.** The contact author has declared that none of the authors has any competing interests.

336 **Disclaimer.** Publisher's note: Copernicus Publications remains neutral with regard to jurisdictional claims in published maps  
337 and institutional affiliations.

338 **Financial support.** This research has been supported by the National Natural Science Foundation of China (grant nos.  
339 91844301, 42005087, and 42005086), Key Research and Development Program of Zhejiang Province (grant nos. 2021C03165,  
340 2022C03084), and the Fundamental Research Funds for the Central Universities (grant no. 2018QNA6008).

## 341 **References**

- 342 Angle, K. J., Crocker, D. R., Simpson, R. M. C., Mayer, K. J., Garofalo, L. A., Moore, A. N., Mora Garcia, S. L., Or, V. W.,  
343 Srinivasan, S., Farhan, M., Sauer, J. S., Lee, C., Pothier, M. A., Farmer, D. K., Martz, T. R., Bertram, T. H., Cappa, C.  
344 D., Prather, K. A., and Grassian, V. H.: Acidity across the interface from the ocean surface to sea spray aerosol, *Proc.*  
345 *Natl. Acad. Sci. U.S.A.*, 118, e2018397118, <https://doi.org/10.1073/pnas.2018397118>, 2021.
- 346 Bertram, A. K., Martin, S. T., Hanna, S. J., Smith, M. L., Bodsworth, A., Chen, Q., Kuwata, M., Liu, A., You, Y., and Zorn,  
347 S. R.: Predicting the relative humidities of liquid-liquid phase separation, efflorescence, and deliquescence of mixed  
348 particles of ammonium sulfate, organic material, and water using the organic-to-sulfate mass ratio of the particle and the  
349 oxygen-to-carbon elemental ratio of the organic component, *Atmos. Chem. Phys.*, 11, 10995-11006,  
350 <https://doi.org/10.5194/acp-11-10995-2011>, 2011.
- 351 Boyer, H. C., Gorkowski, K., and Sullivan, R. C.: In situ pH measurements of individual levitated microdroplets using aerosol  
352 optical tweezers, *Anal. Chem.*, 92, 1089-1096, <https://doi.org/10.1021/acs.analchem.9b04152>, 2020.
- 353 Canagaratna, M. R., Jimenez, J. L., Kroll, J. H., Chen, Q., Kessler, S. H., Massoli, P., Hildebrandt Ruiz, L., Fortner, E.,  
354 Williams, L. R., Wilson, K. R., Surratt, J. D., Donahue, N. M., Jayne, J. T., and Worsnop, D. R.: Elemental ratio  
355 measurements of organic compounds using aerosol mass spectrometry: characterization, improved calibration, and  
356 implications, *Atmos. Chem. Phys.*, 15, 253-272, <https://doi.org/10.5194/acp-15-253-2015>, 2015.
- 357 Ciobanu, V. G.; Marcolli, C.; Krieger, U. K.; Weers, U.; Peter, T. Liquid-Liquid Phase Separation in Mixed Organic/Inorganic  
358 Aerosol Particles. *J. Phys. Chem. A* 2009, 113 (41), 10966–10978.
- 359 Coddens, E. M., Angle, K. J., and Grassian, V. H.: Titration of aerosol pH through droplet coalescence, *J. Phys. Chem. Lett.*,  
360 10, 4476-4483, <https://doi.org/10.1021/acs.jpcclett.9b00757>, 2019. Corral Arroyo, P., David, G., Alpert, P. A., Parmentier,  
361 E. A., Ammann, M., and Signorell, R.: Amplification of light within aerosol particles accelerates in-particle  
362 photochemistry, *Science*, 376, 293-296, <https://doi.org/10.1126/science.abm7915>, 2022.



363 Cosman, L. M., Knopf, D. A., and Bertram, A. K.: N<sub>2</sub>O<sub>5</sub> reactive uptake on aqueous sulfuric acid solutions coated with  
364 branched and straight-chain insoluble organic surfactants, *J. Phys. Chem. A*, 112, 2386, <https://doi.org/10.1021/jp710685r>,  
365 2008.

366 Cui, X., Tang, M., Wang, M., and Zhu, T.: Water as a probe for pH measurement in individual particles using micro-Raman  
367 spectroscopy, *Anal. Chim. Acta.*, 1186, 339089, <https://doi.org/10.1016/j.aca.2021.339089>, 2021.

368 Fang, T., Guo, H., Zeng, L., Verma, V., Nenes, A., and Weber, R. J.: Highly acidic ambient particles, soluble metals, and  
369 oxidative potential: a link between sulfate and aerosol toxicity, *Environ. Sci. Technol.*, 51, 2611-2620,  
370 <https://doi.org/10.1021/acs.est.6b06151>, 2017.

371 Freedman, M. A., Hasenkopf, C. A., Beaver, M. R., and Tolbert, M. A.: Optical properties of internally mixed aerosol particles  
372 composed of dicarboxylic acids and ammonium sulfate, *J. Phys. Chem. A*, 113, 13584-13592,  
373 <https://doi.org/10.1021/jp906240y>, 2009.

374 Freedman, M. A.: Phase separation in organic aerosol, *Chem. Soc. Rev.*, 46, 7694-7705, <http://doi.org/10.1039/C6CS00783J>,  
375 2017.

376 Freedman, M. A.: Liquid-liquid phase separation in supermicrometer and submicrometer aerosol particles, *Acc. Chem. Res.*,  
377 53, 1102-1110, <https://doi.org/10.1021/acs.accounts.0c00093>, 2020.

378 Gong, Z. Y., Pan, Y. L., Videen, G., and Wang, C. J.: Optical trapping and manipulation of single particles in air: principles,  
379 technical details, and applications, *J. Quant. Spectrosc. Ra.*, 214, 94-119, <https://doi.org/10.1016/j.jqsrt.2018.04.027>,  
380 2018.

381 Gorkowski, K., Donahue, N. M., and Sullivan, R. C.: Emulsified and liquid-liquid phase-separated states of alpha-pinene  
382 secondary organic aerosol determined using aerosol optical tweezers, *Environ. Sci. Technol.*, 51, 12154-12163,  
383 <https://doi.org/10.1021/acs.est.7b03250>, 2017.

384 Gorkowski, K., Donahue, N. M., and Sullivan, R. C.: Aerosol optical tweezers constrain the morphology evolution of liquid-  
385 liquid phase-separated atmospheric particles, *Chem*, 6, 204-220, <https://doi.org/10.1016/j.chempr.2019.10.018>, 2020.

386 Guo, H., Liu, J., Froyd, K. D., Roberts, J. M., Veres, P. R., Hayes, P. L., Jimenez, J. L., Nenes, A., and Weber, R. J.: Fine  
387 particle pH and gas-particle phase partitioning of inorganic species in Pasadena, California, during the 2010 CalNex  
388 campaign, *Atmos. Chem. Phys.*, 17, 5703-5719, <https://doi.org/10.5194/acp-17-5703-2017>, 2017.

389 Kucinski, T. M., Dawson, J. N., and Freedman, M. A.: Size-Dependent Liquid-Liquid Phase Separation in Atmospherically  
390 Relevant Complex Systems, *J. Phys. Chem. Lett.*, 10, 6915-6920, <https://doi.org/10.1021/acs.jpcclett.9b02532>, 2019.

391 Kucinski, T. M., Ott, E.-J. E., and Freedman, M. A.: Flash Freeze Flow Tube to Vitrify Aerosol Particles at Fixed Relative  
392 Humidity Values, *Anal. Chem.*, 92, 5207-5213, <https://doi.org/10.1021/acs.analchem.9b05757>, 2020.

393 Kucinski, T. M., Ott, E. E., and Freedman, M. A.: Dynamics of liquid-liquid phase separation in submicrometer aerosol, *J.*  
394 *Phys. Chem. A*, 125, 4446-4453, <https://doi.org/10.1021/acs.jpca.1c01985>, 2021.

395 Lam, H. K., Xu, R., Choczynski, J., Davies, J. F., Ham, D., Song, M., Zuend, A., Li, W., Tse, Y. L. S., and Chan, M. N.:  
396 Effects of liquid-liquid phase separation and relative humidity on the heterogeneous OH oxidation of inorganic-organic  
397 aerosols: insights from methylglutaric acid and ammonium sulfate particles, *Atmos. Chem. Phys.*, 21, 2053-2066,  
398 <https://doi.org/10.5194/acp-21-2053-2021>, 2021.

399 Li, M., Kan, Y., Su, H., Pöschl, U., Parekh, S. H., Bonn, M., and Cheng, Y. F.: Spatial homogeneity of pH in aerosol  
400 microdroplets, *Chem*, in press, <https://doi.org/10.1016/j.chempr.2023.02.019>, 2023.

401 Lin, H. B., Eversole, J. D., and Campillo, A. J.: Continuous-wave stimulated Raman scattering in microdroplets, *P. Opt. Lett.*,  
402 17, 828-830, <https://doi.org/10.1364/ol.17.000828>, 1992.

403 Losey, D. J., Parker, R. G., and Freedman, M. A.: pH Dependence of Liquid-Liquid Phase Separation in Organic Aerosol, *The*  
404 *Journal of Physical Chemistry Letters*, 7, 3861-3865, [10.1021/acs.jpcclett.6b01621](https://doi.org/10.1021/acs.jpcclett.6b01621), 2016.

405 Losey, D. J., Ott, E. J. E., and Freedman, M. A.: Effects of high acidity on phase transitions of an organic aerosol, *J. Phys.*  
406 *Chem. A*, 122, 3819-3828, <https://doi.org/10.1021/acs.jpca.8b00399>, 2018.

407 Ma, S. S., Chen, Z., Pang, S. F., and Zhang, Y. H.: Observations on hygroscopic growth and phase transitions of mixed 1, 2,  
408 6-hexanetriol/(NH<sub>4</sub>)<sub>2</sub>SO<sub>4</sub> particles: investigation of the liquid-liquid phase separation (LLPS) dynamic process and  
409 mechanism and secondary LLPS during the dehumidification, *Atmos. Chem. Phys.*, 21, 9705-9717,  
410 <https://doi.org/10.5194/acp-21-9705-2021>, 2021.

411 Mahrt, F., Newman, E., Huang, Y., Ammann, M., and Bertram, A. K.: Phase behavior of hydrocarbon-like primary organic  
412 aerosol and secondary organic aerosol proxies based on their elemental oxygen-to-carbon ratio, *Environ. Sci. Technol.*,  
413 55, 12202-12214, <https://doi.org/10.1021/acs.est.1c02697>, 2021.

414 Mikhailov, E. F., Pöhlker, M. L., Reinmuth-Selzle, K., Vlasenko, S. S., Krüger, O. O., Fröhlich-Nowoisky, J., Pöhlker, C.,  
415 Ivanova, O. A., Kiselev, A. A., Kremper, L. A., and Pöschl, U.: Water uptake of subpollen aerosol particles: hygroscopic  
416 growth, cloud condensation nuclei activation, and liquid-liquid phase separation, *Atmos. Chem. Phys.*, 21, 6999-7022,  
417 <https://doi.org/10.5194/acp-21-6999-2021>, 2021.

418 Mitchem, L., Buajareern, J., Ward, A. D., and Reid, J. P.: A strategy for characterizing the mixing state of immiscible aerosol  
419 components and the formation of multiphase aerosol particles through coagulation, *J. Phys. Chem. B*, 110, 13700-13703,  
420 <https://doi.org/10.1021/jp062874z>, 2006.

421 O'Brien, R. E., Wang, B. B., Kelly, S. T., Lundt, N., You, Y., Bertram, A. K., Leone, S. R., Laskin, A., and Gilles, M. K.:  
422 Liquid-liquid phase separation in aerosol particles: imaging at the nanometer scale, *Environ. Sci. Technol.*, 49, 4995-  
423 5002, <https://doi.org/10.1021/acs.est.5b00062>, 2015.

424 O'Haver, T. C.: A pragmatic introduction to signal processing with applications in scientific measurement, Kindle Direct  
425 Publishing, ISBN: 9798611266687, 2022.

426 Ohno, P. E., Qin, Y., Ye, J., Wang, J., Bertram, A. K., and Martin, S. T.: Fluorescence aerosol flow tube spectroscopy to detect  
427 liquid-liquid phase separation, *ACS Earth Space Chem.*, 5, 1223-1232,  
428 <http://doi.org/10.1021/acsearthspacechem.1c00061>, 2021.

429 Ott, E.-J. E., Tackman, E. C., and Freedman, M. A.: Effects of Sucrose on Phase Transitions of Organic/Inorganic Aerosols,  
430 *ACS Earth Space Chem.*, 4, 591-601, <http://doi.org/10.1021/acsearthspacechem.0c00006>, 2020.

431 Petters, M. D. and Kreidenweis, S. M.: A single parameter representation of hygroscopic growth and cloud condensation  
432 nucleus activity, *Atmos. Chem. Phys.*, 7, 1961-1971, <https://doi.org/10.5194/acp-7-1961-2007>, 2007.

433 Preston, T. C. and Reid, J. P.: Accurate and efficient determination of the radius, refractive index, and dispersion of weakly  
434 absorbing spherical particle using whispering gallery modes, *J. Opt. Soc. Am. B*, 30, 2113-2122,  
435 <https://doi.org/10.1364/JOSAB.30.002113>, 2013.

436 Preston, T. C. and Reid, J. P.: Determining the size and refractive index of microspheres using the mode assignments from  
437 Mie resonances, *J. Opt. Soc. Am. A*, 32, 2210-2217, <https://doi.org/10.1364/JOSAA.32.002210>, 2015.

438 Pye, H. O. T., Nenes, A., Alexander, B., Ault, A. P., Barth, M. C., Clegg, S. L., Collett, J. L., Jr., Fahey, K. M., Hennigan, C.  
439 J., Herrmann, H., Kanakidou, M., Kelly, J. T., Ku, I. T., McNeill, V. F., Riemer, N., Schaefer, T., Shi, G., Tilgner, A.,  
440 Walker, J. T., Wang, T., Weber, R., Xing, J., Zaveri, R. A., and Zuend, A.: The acidity of atmospheric particles and clouds,  
441 *Atmos. Chem. Phys.*, 20, 4809-4888, <https://doi.org/10.5194/acp-20-4809-2020>, 2020.

442 Rafferty, A., Vennes, B., Bain, A., and Preston, T. C.: Optical trapping and light scattering in atmospheric aerosol science,  
443 *Phys. Chem. Chem. Phys.*, 25, 7066-7089, <https://doi.org/10.1039/d2cp05301b>, 2023.

444 Redding, B., Schwab, M. J., and Pan, Y. L.: Raman spectroscopy of optically trapped single biological micro-particles, *Sensors*,  
445 15, 19021-19046, <https://doi.org/10.3390/s150819021>, 2015.

446 Reid, J. P., Dennis-Smith, B. J., Kwamena, N. O. A., Miles, R. E. H., Hanford, K. L., and Homer, C. J.: The morphology of  
447 aerosol particles consisting of hydrophobic and hydrophilic phases: hydrocarbons, alcohols and fatty acids as the  
448 hydrophobic component, *Phys. Chem. Chem. Phys.*, 13, 15559-15572, <https://doi.org/10.1039/c1cp21510h>, 2011.

449 Rosenfeld, D., Sherwood, S., Wood, R., and Donner, L.: Climate effects of aerosol-cloud interactions, *Science*, 343, 379-380,  
450 <https://doi.org/10.1126/science.1247490>, 2014.

451 Song, M., Marcolli, C., Krieger, U. K., Zuend, A., and Peter, T.: Liquid-liquid phase separation in aerosol particles: dependence  
452 on O:C, organic functionalities, and compositional complexity, *Geophys. Res. Lett.*, 39, L19801,  
453 <https://doi.org/10.1029/2012GL052807>, 2012.

454 Song, M. J., Marcolli, C., Krieger, U. K., Lienhard, D. M., and Peter, T.: Morphologies of mixed organic/inorganic/aqueous  
455 aerosol droplets, *Faraday Discuss.*, 165, 289-316, <https://doi.org/10.1039/c3fd00049d>, 2013.

456 Stewart, D. J., Cai, C., Nayler, J., Preston, T. C., Reid, J. P., Krieger, U. K., Marcolli, C., and Zhang, Y. H.: Liquid-liquid  
457 phase separation in mixed organic/inorganic single aqueous aerosol droplets, *J. Phys. Chem. A.*, 119, 4177-4190,  
458 <https://doi.org/10.1021/acs.jpca.5b01658>, 2015.

459 Sullivan, R. C., Boyer-Chelmo, H., Gorkowski, K., and Beydoun, H.: Aerosol Optical Tweezers Elucidate the Chemistry,  
460 Acidity, Phase Separations, and Morphology of Atmospheric Microdroplets, *Acc. Chem. Res.*, 11, 2498–2509,  
461 <https://doi.org/10.1021/acs.accounts.0c00407>, 2020.

462 Tilgner, A., Schaefer, T., Alexander, B., Barth, M., Collett, J. L., Fahey, K. M., Nenes, A., Pye, H. O. T., Herrmann, H., and  
463 McNeill, V. F.: Acidity and the multiphase chemistry of atmospheric aqueous particles and clouds, *Atmos. Chem. Phys.*,  
464 21, 13483-13536, <https://doi.org/10.5194/acp-21-13483-2021>, 2021.

465 Tong, Y. K., Meng, X. X. Y., Zhou, B., Sun, R., Wu, Z. J., Hu, M., and Ye, A. P.: Detecting the pH-dependent liquid-liquid  
466 phase separation of single levitated aerosol microdroplets via laser tweezers-Raman spectroscopy, *Front. Phys.*, 10,  
467 <https://doi.org/10.3389/fphy.2022.969921>, 2022.

468 Wade, L. G. and Simek, J. W.: Acidity of alcohols and phenols, in: *Organic Chemistry*,  
469 <https://chem.libretexts.org/@go/page/45234>, 2020.

470 Wang, M., Zheng, N., Zhao, D., Shang, J., and Zhu, T.: Using micro-Raman spectroscopy to investigate chemical composition,  
471 mixing states, and heterogeneous reactions of individual atmospheric particles, *Environ. Sci. Technol.*, 55, 10243-10254,  
472 <https://doi.org/10.1021/acs.est.1c01242>, 2021.

473 Weber, R. J., Guo, H. Y., Russell, A. G., and Nenes, A.: High aerosol acidity despite declining atmospheric sulfate  
474 concentrations over the past 15 years, *Nat. Geosci.*, 9, 282-285, <https://doi.org/10.1038/ngeo2665>, 2016.

475 You, Y., Renbaum-Wolff, L., and Bertram, A. K.: Liquid-liquid phase separation in particles containing organics mixed with  
476 ammonium sulfate, ammonium bisulfate, ammonium nitrate or sodium chloride, *Atmos. Chem. Phys.*, 13, 11723-11734,  
477 <https://doi.org/10.5194/acp-13-11723-2013>, 2013.

478 You, Y., Smith, M. L., Song, M., Martin, S. T., Bertram, A. K.: Liquid-liquid phase separation in atmospherically relevant  
479 particles consisting of organic species and inorganic salts, *Int. Rev. Phys. Chem.*, 33 (1), 43–77,  
480 <http://doi.org/10.1080/0144235X.2014.890786>, 2014.

481 Young, A. H., Keene, W. C., Pszenny, A. A. P., Sander, R., Thornton, J. A., Riedel, T. P., and Maben, J. R.: Phase partitioning  
482 of soluble trace gases with size-resolved aerosols in near-surface continental air over northern Colorado, USA, during  
483 winter, *J. Geophys. Res.: Atmospheres*, 118, 9414-9427, <https://doi.org/10.1002/jgrd.50655>, 2013.

484 Zheng, G., Su, H., Wang, S., Andreae, M., Pöschl, U., and Cheng, Y.: Multiphase buffer theory explains contrasts in  
485 atmospheric aerosol acidity, *Science*, 369, 1374-1377, <https://doi.org/10.1126/science.aba3719>, 2020.

486 Zhou, Q., Pang, S.-F., Wang, Y., Ma, J.-B., and Zhang, Y.-H.: Confocal Raman studies of the evolution of the physical state  
487 of mixed phthalic acid/ammonium sulfate aerosol droplets and the effect of substrates, *J. Phys. Chem. B*, 118, 6198-6205,  
488 <https://doi.org/10.1021/jp5004598>, 2014.